Development/Plasticity/Repair

Transcranial Low-Intensity Focused Ultrasound Stimulation of the Visual Thalamus Produces Long-Term Depression of Thalamocortical Synapses in the Adult Visual Cortex

Lukas Mesik,[1,2,3] Samuel Parkins,[1,4] Daniel Severin,[1] Bryce D. Grier,[1,3] Gabrielle Ewall,[1,3] Sumasri Kotha,[1] Christian Wesselborg,[1,4] Cristian Moreno,[1] Yanis Jaoui,[1] Adrianna Felder,[1] Brian Huang,[1] Marina B. Johnson,[5] Timothy P. Harrigan,[5] Anna E. Knight,[5] Shane W. Lani,[5] Théo Lemaire,[6] Alfredo Kirkwood,[1,3] Grace M. Hwang,[2,5] and Hey-Kyoung Lee[1,2,3]

[1]Zanvyl-Krieger Mind/Brain Institute, Johns Hopkins University, Baltimore, Maryland 21218, [2]Kavli Neuroscience Discovery Institute, Johns Hopkins University, Baltimore, Maryland 21218, [3]Solomon H. Snyder Department of Neuroscience, Johns Hopkins School of Medicine, Baltimore, Maryland 21205, [4]Cell Molecular Developmental Biology and Biophysics Graduate Program, Johns Hopkins University, Baltimore, Maryland 21218, [5]Johns Hopkins Applied Physics Laboratory, Johns Hopkins University, Laurel, Maryland 20723, and [6]Neuroscience Institute, New York University Langone Health, New York, New York 10016

Transcranial focused ultrasound stimulation (tFUS) is a noninvasive neuromodulation technique, which can penetrate deeper and modulate neural activity with a greater spatial resolution (on the order of millimeters) than currently available noninvasive brain stimulation methods, such as transcranial magnetic stimulation (TMS) and transcranial direct current stimulation (tDCS). While there are several studies demonstrating the ability of tFUS to modulate neuronal activity, it is unclear whether it can be used for producing long-term plasticity as needed to modify circuit function, especially in adult brain circuits with limited plasticity such as the thalamocortical synapses. Here we demonstrate that transcranial low-intensity focused ultrasound (LIFU) stimulation of the visual thalamus (dorsal lateral geniculate nucleus, dLGN), a deep brain structure, leads to NMDA receptor (NMDAR)-dependent long-term depression of its synaptic transmission onto layer 4 neurons in the primary visual cortex (V1) of adult mice of both sexes. This change is not accompanied by large increases in neuronal activity, as visualized using the cFos Targeted Recombination in Active Populations (cFosTRAP2) mouse line, or activation of microglia, which was assessed with IBA-1 staining. Using a model (SONIC) based on the neuronal intramembrane cavitation excitation (NICE) theory of ultrasound neuromodulation, we find that the predicted activity pattern of dLGN neurons upon sonication is state-dependent with a range of activity that falls within the parameter space conducive for inducing long-term synaptic depression. Our results suggest that noninvasive transcranial LIFU stimulation has a potential for recovering long-term plasticity of thalamocortical synapses in the postcritical period adult brain.

Key words: **adult plasticity; LIFU; long-term depression; noninvasive; synaptic plasticity; ultrasound**

Significance Statement

Recovery of adult sensory cortical function is thought to be limited by the developmental decline in cortical plasticity mechanisms. In particular, thalamocortical (TC) synapses in the primary sensory cortices lose their ability to undergo experience-dependent plasticity quite early in postnatal development. As such, recovery of adult sensory cortical function is often accompanied by restoration of thalamocortical plasticity. Here we used a noninvasive transcranial low-intensity focused ultrasound (LIFU) stimulation, which can produce neuromodulation of localized structures deep in the brain, to elicit long-term depression of TC synapses in the primary visual cortex of adult mice. Our results suggest that transcranial LIFU stimulation could be a useful therapeutic that can produce long-term plasticity of neural circuits to restore adult brain functions.

Received April 30, 2023; revised Dec. 13, 2023; accepted Jan. 30, 2024.

Author contributions: L.M., S.W.L., G.M.H., and H-K.L. designed research; L.M., S.P., D.S., B.D.G., G.E., S.K., C.W., C.M., Y.J., A.F., B.H., M.B.J., T.P.H., A.E.K., G.M.H., and H-K.L. performed research; L.M., S.P., D.S., B.D.G., G.E., S.K., C.W., G.M.H., and H-K.L. analyzed data; S.K. and T.L. contributed unpublished reagents/analytic tools; G.M.H. and H-K.L. wrote the paper.

This work was supported by NIH Grant R21-EY031265 and Johns Hopkins Discovery Award to H-K.L. and GMH, Kavli Neuroscience Discovery Institute Distinguished Postdoctoral Fellowship to L.M., NIH predoctoral fellowship F31-EY031946 to S.P., and NIH Grant R01-EY012124 to A.K. The authors would like to thank Dr. Philip Feurtado for helping with some of the LIFU stimulations.

The authors declare no competing financial interests.

B.D.G.'s present address: Wu Tsai Neuroscience Institute, Stanford University, Stanford, California 94305.

G.M.H.'s present address: National Institute of Neurological Disorders and Stroke, National Institutes of Health, Rockville, Maryland 20852.

Correspondence should be addressed to : Grace Hwang at grace.hwang@nih.gov or Hey-Kyoung Lee at heykyounglee@jhu.edu.

https://doi.org/10.1523/JNEUROSCI.0784-23.2024

Introduction

Traditional methods of brain stimulation have largely relied on electrical stimulation through implanted electrodes, which confer temporal precision and defined spatial localization. However, these methods require surgical implantation and suffer from the potential damage of neural tissue from direct contact with the electrodes. To address these drawbacks, several noninvasive methods for neural modulation have been developed, such as transcranial magnetic stimulation (TMS) (Thielscher and Kammer, 2002) and transcranial direct current stimulation (tDCS) (Woods et al., 2016), but their utility is limited by low spatial resolutions (≥1 cm diameter) (Wagner et al., 2007) and superficial cortical stimulations (Wagner et al., 2007; Siebner et al., 2009). Transcranial focused ultrasound stimulation (tFUS) is a rather unique noninvasive neuromodulation method with a finer spatial resolution (in the range of millimeters) and penetration capacity for deep brain neuromodulation (Baek et al., 2017; Tyler et al., 2018; Dell'Italia et al., 2022). tFUS has been used in different preparations to activate neurons and elicit movement or behavioral changes (Tyler, 2011; Dell'Italia et al., 2022) by modulating neuronal activity through eliciting action potentials (Tufail et al., 2010; Tyler et al., 2018) or suppressing activity (Yoo et al., 2011; Dell'Italia et al., 2022). However, a current gap in knowledge is whether tFUS can modulate neuronal activity to drive long-term plasticity, especially in adult circuits with limited capacity. This understanding is much needed for the development of tFUS-based therapeutics aimed at recovering adult brain functions. We address this by using the thalamocortical circuit in the primary visual cortex (V1) of adult mice as a model.

V1 has been used as a model of cortical plasticity in which the basic principles of experience-dependent plasticity have been elucidated. One of the key properties of cortical plasticity is that it has a defined critical period, which limits the ability of cortical circuits to adapt to changes in sensory experience to an early developmental period (Lee et al., 2005; Hooks and Chen, 2020). At a cellular level, synaptic plasticity has been studied across all the cortical layers, and an emerging consensus is that thalamocortical (TC) plasticity terminates early in postnatal development (Crair and Malenka, 1995; Dudek and Friedlander, 1996; Desai et al., 2002; Jiang et al., 2007; Barkat et al., 2011), while plasticity of other layers often persists through adulthood (Feldman et al., 1998; Desai et al., 2002; Goel and Lee, 2007; Jiang et al., 2007). These studies suggest that the loss of TC plasticity may be a precursor for the closure of the critical period. In support of this idea, recovery of cortical plasticity in adults is often accompanied by restoration of TC plasticity (Montey and Quinlan, 2011; Yu et al., 2012; Petrus et al., 2014; Chung et al., 2017; Rodriguez et al., 2018). Such findings suggest that induction of TC plasticity may benefit the functional recovery of the adult sensory cortex.

Here we investigated whether noninvasive tFUS of dLGN would elicit TC synaptic plasticity in the adult V1. Development of such a tool would have wide applications across different brain areas, as currently there is a paucity of methods available for noninvasive stimulation of deep brain structures like dLGN. We demonstrate that a pattern of low-intensity focused ultrasound (LIFU) stimulation targeted to dLGN through intact skin and skull of anesthetized adult mice produces NMDAR-dependent long-term depression of TC synaptic transmission measured in V1 layer 4 (L4) neurons. This was not accompanied by changes in cFosTRAP2-mediated gene expression, which detects large abrupt increases in activity (Guenthner et al., 2013), or a marker of microglia, which is upregulated following neuroinflammation (Muzio et al., 2021). Using simulations based on the intramembrane cavitation model of ultrasound neuromodulation (Lemaire et al., 2019), we found that the LIFU stimulation protocol is predicted to generate different firing patterns in dLGN neurons dependent on their state. Our results suggest that transcranial LIFU stimulation can generate long-term plasticity of TC synapses in the adult V1, which could benefit the development of noninvasive therapeutics to aid in functional recovery.

Materials and Methods

Animals

Mice of both sexes were used in this study and reared in a normal 12-hour light/12-hour dark cycle. VGluT2-Cre (*Slc17a6*$^{tm2(cre)Lowl}$/J, Jax mice stock# 016963; RRID:IMSR_JAX:016963) mice were used for targeting channelrhodopsin-2 (ChR2) expression in dLGN. cFosTRAP2 (*Fos*$^{tm2.1(icre/ERT2)Luo}$/J, Jax mice stock# 030323; RRID:IMSR_JAX:030323) mice were crossed with Ai14 (B6.Cg-*Gt(ROSA)26Sor*$^{tm14(CAG-tdTomato)Hze}$/J, Jax mice stock# 007914; RRID:IMSR_JAX:007914) to generate cFosTRAP2;Ai14 mice for histological analysis of neuronal activation. All animal procedures conform to the guidelines of the US Department of Health and Human Services Office of Laboratory Animal Welfare and were approved by the Institutional Animal Use and Care Committee at Johns Hopkins University.

In vivo stereotaxic injections to express channelrhodopsin-2 (ChR2) in dLGN

VGluT2-Cre mice were used to specifically express ChR2 bilaterally in dLGN using targeted injections. Adult mice were anesthetized using isoflurane (5% induction, 1–2% maintenance) and mounted on a stereotaxic instrument (Kopf). An incision was made along the midline and the skin was retracted to the sides to expose the skull. After stereotaxic leveling, small craniotomies were made in both hemispheres, centered 2 mm lateral and 2.3 mm posterior of Bregma. AAV9.Ef1alpha.dflox.hChR2(H134R) mCherry.WPRE.hGH (Addgene 20297-AAV9, titer 10^{13} GC/ml; RRID:Addgene_20297) diluted 1:1 in sterile saline (~200 nl) was then loaded into a glass pipette using a syringe pump (Harvard Apparatus) and injected bilaterally into dLGN (coordinates relative to Bregma: 2 mm lateral, 2.3 mm posterior and 2.6 mm depth). The skin was sutured, and mice were recovered on a heated pad (30°C) and returned to the animal colony housed with approximately 2–4 of same-sexed mice for about 2–4 weeks and prepared for LIFU stimulation. Mice were monitored daily to ensure no postsurgery infection or signs of distress.

Bilateral enucleation

Mice were bilaterally enucleated at least the day before LIFU stimulation of dLGN to prevent visually driven activity through the visual circuit. Mice were put under isoflurane anesthesia (5% induction, 2% maintenance) and mounted on a stereotaxic apparatus (Kopf) without the use of ear bars. The head was rotated sideways to facilitate easy eye access and the eye was popped out of the socket using curved tweezers. The eye was then grabbed at the base by the optic nerve, twisted around at least three times to prevent bleeding, and cut off using surgical scissors. Finally, eyelids were glued together using tissue adhesive (Vetbond).

LIFU stimulation

The LIFU stimulation device used was developed by the Johns Hopkins Applied Physics Laboratory (JHU/APL) and utilized a single-element focused ultrasound transducer with a center frequency of 0.5 MHz (BII-7651H/500IMTS, Benthowave Instruments Inc.) fitted with an individually tailored acoustic waveguide. While the design frequency for the transducer is 0.5 MHz, acceptance testing showed that the optimal power efficiency occurred at 0.59 MHz. This frequency was found stable and was then used for all procedures to minimize electrical impedance

mismatches and limit transducer heating. While this device is capable of high-intensity focused ultrasound (HIFU), the stimulation parameters of LIFU were limited to time averaged intensity (I_{SPTA}) < 720 mW/cm^2, and pulse average intensity (I_{SPPA}) < 190 W/cm^2 or mechanical index (MI) < 1.9. These parameters are in line with current FDA requirements of acoustic output (FDA, 2023); hence it is considered LIFU stimulation.

The APL group extensively characterized and demonstrated the ability of the LIFU system to focus ultrasound stimulation deep within the tissue below the skull (Lani et al., 2017, 2018; Hwang et al., 2018; Tyler et al., 2018). The ultrasonic transducer generates an acoustic focus in water 22 mm below the face of the transducer with a focal diameter of 2.2 mm and focal length of 7.6 mm at the half power points (Fig. 1*A*). To retain and not distort the properties of the focal spot during coupling to the subject, a rigid conical waveguide was fabricated with Conathane EN-11 and EN-4 resin to match the acoustic specific impedance of water. The resin waveguide was form fitted to the transducer face and coupled using ultrasound gel (Medline). Additional details on the waveguide design, fabrication, and testing can be found in (Lani et al., 2018). The transducer with a custom fabricated waveguide is expected to place the focal point near dLGN (Fig. 1*B*). The delivered acoustic intensity was measured and calibrated in a water tank using a calibrated needle hydrophone (Precision Acoustics model NH0500) with the waveguide present to ensure levels were within protocols.

On the day of the LIFU stimulation, mice were put under isoflurane anesthesia (5% induction, 1–1.5% maintenance) and mounted on a stereotaxic instrument (Kopf). Hair was removed from the head using Nair hair removal lotion. A marker was used to draw a targeting cross centered approximately over the left or right dLGN (using the midline and estimated position of lambdoid suture for guidance). For a group of mice, NMDAR antagonist D-4-[(2E)-3-phosphono-2-propenyl]-2-piperazinecarboxylic acid (D-CPP; Tocris Biosciences catalog #1265) was injected intraperitoneally (i.p., 10 mg/kg) 10–20 min prior to the LIFU stimulation to test the role of NMDARs. The ultrasonic transducer with the waveguide was mounted on a multi-axis positioning stage and placed over the head of the mouse for precision sonication. The rigidity and small contact point of the waveguide (8 mm diameter) allowed for visual alignment of the transducer over the anatomical markings of the head. The skin was covered by ultrasound gel (Medline) and the contact point of the waveguide was carefully centered over the targeting cross and lowered until tight contact with the skin. LIFU stimulation was started after confirming good skin contact, absence of bubbles in the ultrasound gel, and stable level of anesthesia.

LIFU stimulation parameters were initially designed based on a prior paper that reported transcranial ultrasound stimulation (Tufail et al., 2010). We subsequently used the SONIC model to determine the predicted neural activation patterns (see *Computational modeling of thalamocortical neural activity upon sonication* section below). To generate the wave train of tone bursts, two function generators were used in series. The first function generator (Agilent model #33510B) set the pulse repetition frequency of 500 Hz and triggered the second function generator (Tektronix model #AFG3021B) to send a tone burst of 50 pulses or a tone burst duration of 0.0847 msec. The resulting wave train was passed to a high voltage amplifier (MiniCircuits model LZY-22+).

LIFU stimulation parameters used in this study are the following: waveform center frequency = 0.59 MHz, peak intensity = 2.4 W/cm^2, time average intensity (I_{SPTA}) = 99–109.5 mW/cm^2, pulse repetition frequency (PRF) = 500 Hz, cycles per pulse = 50 (at a duty cycle of 4.24%), peak pressure = 270 kPa, MI = 0.35–0.37, and volts out = 25–30 V. Each mouse was subjected to unilateral LIFU stimulation targeting left or right dLGN using these parameters for a total duration of 1 h under isoflurane anesthesia.

Brain slice preparation and whole-cell recordings

After about 4 weeks following the unilateral LIFU stimulation, which is about 6–7 weeks after the AAV-dflox-ChR2-mCherry injection to allow sufficient expression of ChR2 at dLGN terminals in V1, mice were euthanized for brain slice electrophysiology. Each mouse was deeply anesthetized using isoflurane vapors until the absence of corneal and toe pinch reflexes, then transcardially perfused with ice-cold dissection buffer (212.7 mM sucrose, 10 mM dextrose, 2.6 mM KCl, 1.23 mM $NaH_2PO_4•H_2O$, 26 mM $NaHCO_3$, 3 mM $MgCl_2$, and 1 mM $CaCl_2$) and decapitated. A block of the brain containing V1 was dissected and sliced on a vibratome (model VT1200, Leica) in ice-cold dissection buffer saturated with 95% O_2/5% CO_2 to obtain 300 µm thick coronal slices. Slices from each hemisphere were collected and placed separately in a holding chamber containing artificial cerebrospinal fluid (ACSF: 124 mM NaCl, 5 mM KCl, 1.25 mM $NaH_2PO_4•H_2O$, 10 mM dextrose, 1.5 mM $MgCl_2$, and 2.5 mM $CaCl_2$) continually bubbled with 95% O_2/5% CO_2 and recovered for ∼1 h at room temperature.

Brain slices were transferred to a submersion-type recording chamber mounted on a fixed stage of an upright microscope with oblique infrared illumination (model E600FN, Nikon) and were continually supplied with ACSF bubbled with 95% O_2/5% CO_2 at a flow rate of ∼2 ml/min. Whole-cell patch-clamp recordings were performed on L4 neurons in V1 which were postsynaptic to ChR2-expressing dLGN axon terminals. To measure the strength of ChR2-evoked synaptic transmission, extracellular Ca^{2+} was replaced with 4 mM Sr^{2+}, and Mg^{2+} concentration was raised to 4 mM. To ensure that LED-evoked responses were monosynaptic, recordings were performed in the presence of 1 µM TTX and 100 µM 4-AP. ChR2 activation was achieved by delivering a 5 msec duration pulse of LED (455 nm, Thor Labs) light through the objective lens. Whole-cell recording electrodes were filled with Cs-gluconate internal solution (130 mM Cs-gluconate, 10 mM HEPES, 8 mM KCl, 1 mM EGTA, 4 mM disodium-ATP, 10 mM disodium-phosphocreatine, 0.5 mM sodium-GTP, and 5 mM lidocaine N-ethyl bromide; pH 7.4, 275–285 mOsm). L4 neurons were voltage-clamped at −80 mV holding potential. Recorded cells were routinely filled with biocytin (1 mg/ml; Sigma-Aldrich, catalog #B4261) to confirm their location post hoc. All recordings were amplified using an amplifier (model 700B, Molecular Devices), digitized at 10 kHz by a data acquisition board (National Instruments), and acquired using a custom-made IGOR program (WaveMetrics).

Analysis of LED-evoked Sr^{2+}-miniature excitatory postsynaptic currents (Sr^{2+}-mEPSCs)

Cells exhibiting series resistance (R_s) ≤ 25 MΩ, input resistance (R_{in}) ≥ 200 MΩ, and RMS noise ≤2 were used for final analysis. The detection threshold for selecting mEPSCs was set at three times the RMS noise and analyzed following previous studies (Petrus et al., 2014, 2015; Rodriguez et al., 2018; Chokshi et al., 2019). There was no statistical difference in the recording variables across the two hemispheres (R_s: CTL = 20.6 ± 1.26 MΩ, LIFU = 20.5 ± 0.64 MΩ, two-tailed unpaired *t* test, $t = 0.0976$, $p = 0.9229$; R_{in}: CTL = 576 ± 71.1 MΩ, LIFU = 548 ± 43.7 MΩ, two-tailed unpaired *t* test, $t = 0.3511$, $p = 0.7279$; RMS noise: CTL = 1.76 ± 0.064, LIFU = 1.71 ± 0.034, two-tailed Mann–Whitney test, $p = 0.2044$). In brief, a 400 msec window before the LED stimulation was used for collecting spontaneous mEPSCs from each trace. Another 400 msec window was set at 50 msec following the LED stimulation to collect postLED events, which includes LED-evoked Sr^{2+}-desynchronized mEPSCs. From each cell, 50–200 events were collected from pre-LED and postLED analysis windows. Analysis of mEPSCs was done using a custom-made MATLAB script (https://github.com/bdgrier). Cells with a <2 Hz difference in the frequency of events before and after LED stimulation were excluded from the final analysis because they reflect cells with insufficient LED-evoked desynchronized events. Spontaneous mEPSCs (pre-LED events) were mathematically subtracted from the postLED events as detailed in prior studies (Petrus et al., 2014, 2015; Rodriguez et al., 2018; Chokshi et al., 2019) to obtain the average amplitude of LED-evoked Sr^{2+}-mEPSCs using the following equation:

$$\frac{[(A_{post} \cdot F_{post}) - (A_{pre} \cdot F_{pre})]}{(F_{post} - F_{pre})},$$

where, A_{post} is the average amplitude of postLED events, F_{post} is the average frequency of postLED events, A_{pre} is the average amplitude of pre-LED events, and F_{pre} is the average frequency of pre-LED events.

cFosTRAP2 induction. For cFosTRAP2-mediated neural activity measurement, we used cFosTRAP2;Ai14 mice. The day before the

experiment, 4-hydroxytamoxifen (4OHT) was freshly prepared by dissolving 10 mg 4OHT (Sigma, catalog #H7904 or Hello Bio, catalog #HB2508) in 1 ml of ethanol and then mixing the solution with corn oil 1:1 and allowing ethanol to evaporate, resulting in 10 mg/ml 4OHT in corn oil.

To validate the cFosTRAP2;Ai14 model, we examined tdTomato induction following monocular enucleation (ME). The enucleation method was the same as described above, except only performed unilaterally. Mice were subsequently placed in a darkroom (dark exposure) overnight to remove visually driven activity and brought out to light for 2 h with an injection of 4OHT (50 µg/g 4OHT, i.p.) as detailed below. After the 2 h of light exposure, mice were returned to the darkroom to prevent further visually driven activity through the open eye. After 1 week to allow for the sufficient expression of tdTomato, mice were processed for histology as described below.

For LIFU stimulation experiments, cFosTRAP2;Ai14 mice were bilaterally enucleated at least 1 d before the experiment and then underwent LIFU stimulation under isoflurane anesthesia as described above with the transducer centered over left or right dLGN. Immediately following the stimulation, the mice were weighed and injected intraperitoneally with 5 µl/g of 10 mg/ml 4OHT (i.e., 50 µg/g 4OHT). The mice were then returned to their home cages for 1 week to allow sufficient expression of tdTomato before being sacrificed for histology.

Immunohistochemical detection of cFosTRAP2;Ai14 and activated microglia. After 7 d following LIFU stimulation and cFosTRAP2 induction, mice were deeply anesthetized using isoflurane vapors. After the disappearance of the corneal reflex, mice were kept under deep anesthesia via a supply of isoflurane vapors through a nose-cone and transcardially perfused with ~5 ml of phosphate buffered saline (PBS, pH 7.4) followed by ~5 ml of 10% formalin solution (Sigma-Aldrich, catalog # HT5012). Mice were then decapitation and the fixed brain was removed for postfixation overnight in formalin solution at 4°C shielded from light. The postfixed brain was coronally sectioned at 100 µm thickness on a vibratome (Vibratome 1,000 plus, Ted Pella) and collected in PBS. We selected 6 sections roughly spaced out (~500 µm intervals) across the brain to cover anterior to posterior areas (Bregma coordinates: roughly between −0.5 and −4 mm) and attempted to match the coronal sections across mice to be consistent. Sections were counterstained with DAPI (1:1,000) followed by two washes in PBS. Sections were then mounted on pre-cleaned slides, coverslipped with Prolong Antifade mounting media (ThermoFisher), nail polish sealed, and stored shielded away from light.

We used IBA-1 as a marker for microglial activation. For LIFU stimulated brains, we used the sections from cFosTRAP2;Ai14 mice prepared as detailed above. IBA-1 staining was done on free-floating sections as described previously (Hovens et al., 2014). Brain sections were pretreated with 0.3% H_2O_2 in PBS for 20 min then washed twice in PBS (10 min each) at room temperature. Sections were then incubated with rabbit anti-IBA1 antibody (rabbit recombinant monoclonal IBA-1 antibody, Abcam, catalog # ab178846) diluted 1:2,500 in PBS with 2% bovine serum albumin and 0.1% Triton X-100 for 3 d at 4°C. Sections were then washed twice in PBS (10 min each) at room temperature, then incubated in Alexa Fluor 488 conjugated goat anti-rabbit IgG antibody diluted 1:500 in PBS with 2% bovine serum albumin and 0.1% Triton X-100 at room temperature for 1 h. Sections were then washed twice in PBS (10 min each) at room temperature. Then counterstained with DAPI (1:1,000 dilution) followed by washes in PBS (2× 10 min each). Sections were then mounted on a pre-cleaned slide, coverslipped after application of Prolong Antifade mounting media (ThermoFisher), nail polish sealed, and stored shield away from light.

Slides were imaged using a confocal microscope (LSM700, Zeiss) with a 10× objective lens and stitched together using a tile function to acquire images of the whole coronal plane from LIFU stimulated brain sections. Acquired images were quantified using FIJI (ImageJ) software. Cell depth analysis was done using a custom-made MATLAB script (https://github.com/heykyounglee/Cell_Depth_Analysis).

Computational modeling of thalamocortical neural activity upon sonication. We modeled the electrical membrane dynamics of a thalamocortical neuron with a Hodgkin-Huxley formalism, describing the evolution of the membrane charge density ($Q_m = C_m \cdot V_m$, where C_m and V_m represent the membrane capacitance and potential, respectively) under the action of a cell-type-specific set of ionic currents. Specifically, this set included a sodium current (I_{Na}), a delayed-rectifier and leakage potassium currents (I_{Kd} and I_{Kl}, respectively), a low-threshold T-type calcium current (I_{CaT}), a mixed cationic current (I_H) and a nonspecific leakage current (I_{Leak}), as in (Destexhe et al., 1996). It was complemented by a constant drive current term I_{drive}, representing a simplified pre-synaptic input to the neuron. It results in the following membrane governing equation:

$$\frac{d(C_m \cdot V_m)}{dt} = -(I_{Na} + I_{Kd} + I_{Kl} + I_{\mathrm{CaT}} + I_H + I_{\mathrm{Leak}}) + I_{\mathrm{drive}}. \quad (1)$$

In this conductance-based model, passive currents are expressed as the product of a constant conductance g_x, and the difference between the membrane potential and a specific reversal potential E_x:

$$\begin{aligned} I_{Kl} &= g_{Kl} \cdot (V_m - E_{Kl}) \\ I_{\mathrm{Leak}} &= g_{\mathrm{Leak}} \cdot (V_m - E_{\mathrm{Leak}}). \end{aligned} \quad (2)$$

while active currents feature an additional gating term (represented by one or multiple gating variables) to capture their voltage and time-dependent conductance:

$$\begin{aligned} I_{Na} &= \overline{g_{Na}} \cdot m^3 h \cdot (V_m - E_{Na}) \\ I_{Kd} &= \overline{g_{Kd}} \cdot n^4 \cdot (V_m - E_{Kd}) \\ I_{\mathrm{CaT}} &= \overline{g_{\mathrm{CaT}}} \cdot s^2 u \cdot (V_m - E_{\mathrm{CaT}}) \\ I_H &= \overline{g_H} \cdot (o + 2(1 - o - c)) \cdot (V_m - E_H). \end{aligned} \quad (3)$$

Values of all conductances and reversal potentials are given in Table 1. The gating of sodium, delayed-rectifier potassium, and calcium currents obey a simple two-state kinetic scheme, whereby gating transitions are regulated by voltage-dependent activation and inactivation rate constants (α_x and β_x, respectively), or by an equivalent steady-state probability ($x_\infty = ((\alpha_x)/(\alpha_x + \beta_x))$) and time constant ($\tau_x = ((1)/(\alpha_x + \beta_x))$):

$$\begin{aligned} \frac{dm}{dt} &= \alpha_m(V_m) \cdot (1 - m) - \beta_m(V_m) \cdot m \\ \frac{dh}{dt} &= \alpha_h(V_m) \cdot (1 - h) - \beta_h(V_m) \cdot h \\ \frac{dn}{dt} &= \alpha_n(V_m) \cdot (1 - n) - \beta_n(V_m) \cdot n \\ \frac{ds}{dt} &= \frac{s_\infty(V_m) - s}{\tau_s} \\ \frac{du}{dt} &= \frac{u_\infty(V_m) - u}{\tau_u}. \end{aligned} \quad (4)$$

Table 1. Conductances and reversal potentials of the constituent ionic currents of the thalamocortical neuron model

	Maximal conductance (mS/cm^2)		Reversal potential (mV)	
Current type	Symbol	Value	Symbol	Value
Sodium (I_{Na})	$\overline{g_{Na}}$	90	E_{Na}	+50
Delayed rectifier potassium (I_{Kd})	$\overline{g_{Kd}}$	10	E_K	−90
Leakage potassium (I_{Kl})	g_{Kl}	0.0138		
Low-threshold T-type calcium (I_{CaT})	$\overline{g_{\mathrm{CaT}}}$	2	E_{Ca}	+120
Mixed cationic (I_H)	$\overline{g_H}$	0.0175	E_H	−40
Nonspecific leakage (I_{Leak})	g_{Leak}	0.01	E_{Leak}	−70

The gating of the mixed cationic current obeys a more complex kinetic scheme, depending on both voltage and intracellular calcium concentration $[Ca_i]$, as described in detail in (Destexhe et al., 1996):

$$\begin{aligned}\frac{do}{dt} &= \alpha_o(V_m)\cdot c - \beta_o\cdot o - k_3\cdot o\cdot(1-P_0) + k_4\cdot(1-o-c)\\ \frac{dc}{dt} &= \beta_o(V_m)\cdot o - \alpha_o(V_m)\cdot c\\ \frac{dP_0}{dt} &= k_2\cdot(1-P_0) - k_1\cdot P_0\cdot[Ca_i]^2.\end{aligned} \quad (5)$$

Here, $1 - P_0$ represents the fraction of a calcium regulating factor bound by intracellular calcium, while the constants $k_1, \ldots k_4$ [defined as in (Destexhe et al., 1996)] govern transitions between the different gating states. The intracellular calcium concentration is regulated by the combination of a first order decay and an influx due to the inward calcium current I_{CaT}:

$$\frac{d[Ca_i]}{dt} = \frac{[Ca_i]_0 - [Ca_i]}{\tau_{Ca}} - \frac{k}{2Fd}\cdot I_{CaT}, \quad (6)$$

where the equilibrium intracellular calcium concentration $[Ca_i]_0$ is set to 50 nM, the intracellular calcium decay time constant τ_{Ca} to 5 ms [as in (Destexhe et al., 1996)], and the effective depth of the calcium influx shell d to 100 nm [as in (Plaksin et al., 2016)], while F represents the Faraday constant and k the conversion constant from molar units to current density units.

The gating transition functions of sodium and potassium currents (α_m, β_m, α_h, β_h, α_n, and β_n) were taken from (Pospischil et al., 2008) and those of the calcium current (s_∞, τ_s, u_∞ and τ_u) from (Plaksin et al., 2016). The transition rate functions of the mixed cationic current (α_o and β_o) were derived from equivalent activation steady-state and time constant functions found in (Huguenard and McCormick, 1992).

To simulate the impact of LIFU stimulation on thalamocortical activity, we incorporated this point-neuron model into the SONIC paradigm (Lemaire et al., 2019), a validated, open-source, and computationally efficient implementation of the Neuronal Intramembrane Cavitation Excitation (NICE) model (Plaksin et al., 2014). Under this paradigm, transmembrane ionic currents are re-expressed as a function of an effective membrane potential V_m^*, which captures the cycle-averaged impact of oscillatory membrane perturbations by the acoustic pressure:

$$I_j = g_x\cdot(V_m^* - E_x). \quad (7)$$

Analogously, gating transitions are re-expressed as a function of effective rate constants α_x^* and β_x^*:

$$\frac{dx}{dt} = \alpha_x^*\cdot(1-x) - \beta_x^*\cdot x. \quad (8)$$

These effective variables were pre-tabulated using default geometrical and biomechanical parameters for the underlying "bilayer sonophore model," and assuming a sonophore coverage fraction set to 50%.

Finally, to enable the simulation of neural dynamics upon sustained (i.e., neuroplasticity-inducing) LIFU exposure, we augmented the dimensionality of SONIC simulation protocols with an additional layer of temporal granularity enabling the repetition of LIFU pulse trains at a low (typically sub-Hz) frequency. The conductances and reversal potentials of the constituent ionic currents used for simulating thalamocortical dLGN neuron is detailed in Table 1. Python code for the simulation is publicly available at: https://github.com/tjjlemaire/PySONIC

Experimental design and statistical analysis of data. The experimental design was done to allow within-subject comparisons (the unstimulated hemisphere served as a control for the LIFU stimulated hemisphere). Sample sizes were determined based on prior (Petrus et al., 2014, 2015; Chokshi et al., 2019) and preliminary studies. Statistical analyses were done using Prism 9 (Graph Pad) software. For two group comparisons of normally distributed data sets, t tests were used for most experiments except for the cell depth analysis, which used repeated measures two-way ANOVA. Data sets not normally distributed (assessed using the Shapiro–Wilk test with $p < 0.05$) were compared using a nonparametric Mann–Whitney test. Outliers were removed from the final data set using the ROUT test with Q = 1% cutoff (only one data set, IBA-1 cell density in the cortex, had 2 outliers as noted in the figure legend). Data are presented as mean ± SEM. The specific tests used are specified and detailed in the figure legends. $P < 0.05$ was taken as statistically significant. Final data sets are available on the Mendeley Data (DOI: 10.17632/zk33z4vc8k.1).

Code accessibility. Custom-made analysis codes and the SONIC simulation codes are publicly available through GitHub (www.github.com) with the links provided above.

Results

LIFU stimulation of dLGN results in NMDAR-dependent long-term depression of dLGN synapses in V1 L4

To investigate whether tFUS can produce long-term synaptic plasticity of TC inputs from dLGN to V1 L4, AAV carrying a Cre-dependent ChR2 was injected bilaterally in dLGN of VGluT2-Cre mice. VGluT2 is highly expressed in the thalamic nuclei, including dLGN (Coleman et al., 2010). Hence the use of VGluT2-Cre allows the expression of ChR2 in dLGN and their axon terminals in V1. After about 2–4 weeks, mice were prepared for LIFU stimulation using an ultrasound transducer fitted with a waveguide to place the focal spot near dLGN (Fig. 1). Mice were bilaterally enucleated at least the day before to prevent visually driven activity in the dLGN to V1 circuit. The parameters used for the LIFU stimulation were modified from a prior study, which reported cFos and brain-derived neurotrophic factor (BDNF) induction using a different ultrasound transducer (Tufail et al., 2010). While the published study did not find sufficient penetration of ultrasound waves across the white matter (Tufail et al., 2010), our transducer produces a focused beam of ultrasound (Fig. 1*A*), which is predicted to penetrate deeper into the brain tissue (Fig. 1*B*). Mice were anesthetized and head-fixed, and the LIFU transducer was positioned above the coordinates for dLGN using a multi-axis positioning stage. The fur on the head was removed and the transducer with the attached waveguide was placed firmly on the exposed skin with ultrasound gel (Fig. 2*A*). The skin of the mouse is thin, and we were able to use the visible sagittal and lambdoid sutures on the skull below as anatomical landmarks to position the tip of the waveguide. LIFU stimulation (see Methods for details) was delivered to one hemisphere for 1 h. The mouse was returned to the home cage after recovery from anesthesia and kept for an additional 4 weeks before being used for ex vivo brain slice electrophysiology (Fig. 2*B*). L4 principal neurons in V1 of both hemispheres (LIFU stimulated and nonstimulated) were recorded under whole-cell voltage-clamp configuration. To compare the strength of dLGN synapses on L4 neurons without the confounds of potential differences in the density of ChR2 expressing dLGN terminals, the expression level of ChR2, or the intensity of light used for their activation, we measured LED-evoked Sr^{2+}-mEPSCs as in our prior studies (Petrus et al., 2014, 2015; Rodriguez et al., 2018; Chokshi et al., 2019). We verified the expression of ChR2 by imaging the mCherry tag and confirmed the location of the recorded neurons by processing for biocytin, which was added to the internal solution (Fig. 2*C*). We found that the strength of dLGN inputs to V1 L4 in the LIFU stimulated hemisphere, quantified as the average amplitude of LED-evoked Sr^{2+}-mEPSCs, was significantly

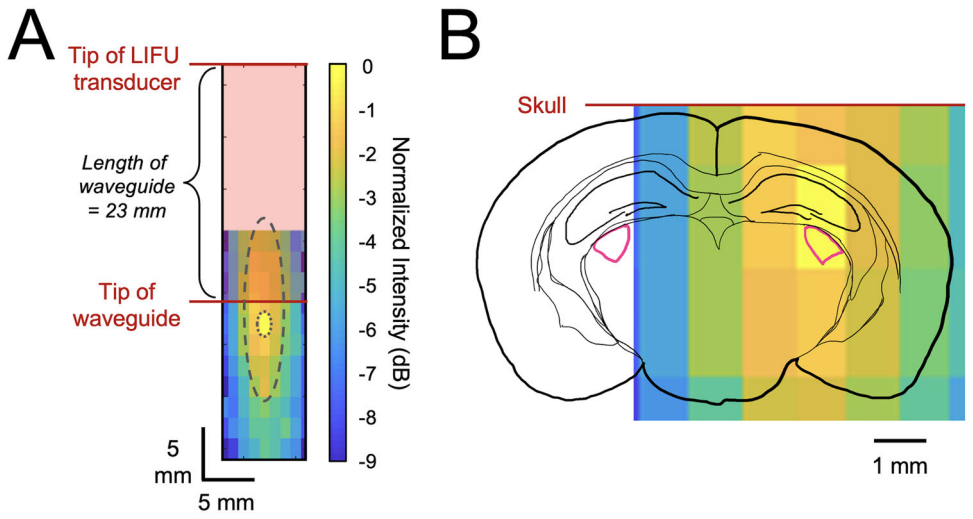

Figure 1. LIFU transducer acoustic intensity profile. ***A***, Normalized acoustic intensity profile (normalized to the peak intensity) of the LIFU transducer measured in a water tank using a calibrated needle hydrophone. The tip of the transducer and the tip of the custom-fabricated waveguide (23 mm length) are shown. The intensity profile was measured without the waveguide present; however, the focal pattern remains the same with part of the focal pattern occurring within the waveguide as depicted in the figure because the waveguide matches the acoustic specific impedance of water. Long dashed gray line outlines −3 dB of maximum acoustic intensity. Short dashed gray line outlines 90% of maximum acoustic intensity. ***B***, The tip of the waveguide is placed flat on the head of a mouse after removing the fur to expose the skin. The acoustic intensity profile in (***A***) is overlaid with a traced outline of a mouse brain taken from a mouse brain atlas [Plate 50, Bregma −2.3 mm in (Paxinos and Franklin, 2001)] to show the expected location of the peak acoustic energy inside the skull. The boundaries of dLGN are outlined in pink. The center of the LIFU transducer was placed approximately ∼2 mm lateral to the midline and the lambdoid suture, which is visible through the exposed skin, was used as a guide for estimating the anterior-posterior target location.

depressed compared to that recorded in the control hemisphere (CTL: 12.7 ± 0.65 pA, $n = 11$ cells; LIFU: 10.7 ± 0.51 pA, $n = 21$ cells; 4 mice; two-tailed unpaired t test with Welch's correction: $t = 2.372$, $p = 0.0268$; Fig. 2*D*). This suggests that LIFU stimulation produces long-term synaptic depression, which can be measured at least 4 weeks after induction. The observed synaptic depression was not due to a global depression of synaptic transmission on V1 L4 neurons because we did not observe statistically significant difference in the average amplitude of spontaneous mEPSCs, which were acquired during a time window prior to the LED stimulation (CTL: 12.0 ± 0.63 pA, $n = 11$ cells; LIFU: 11.6 ± 0.41 pA, $n = 21$ cells; 4 mice; two-tailed unpaired t test with Welch's correction: $t = 0.5585$, $p = 0.5833$).

Next, we tested whether the observed long-term synaptic depression was dependent on NMDARs. To do this, we injected the NMDAR antagonist CPP (10 mg/kg, i.p.) 10 to 20 min prior to the 1 h LIFU stimulation in one hemisphere. V1 slices were obtained approximately 4 weeks after the LIFU stimulation with CPP. We found no statistically significant difference in the strength of dLGN inputs to V1 L4, as quantified by the average amplitude of LED-evoked Sr^{2+}-mEPSCs (CTL + CPP: 13.0 ± 0.56 pA, $n = 20$ cells; LIFU + CPP: 13.1 ± 0.44 pA, $n = 21$ cells; 4 mice; two-tailed Mann–Whitney test: $p = 0.6891$; Fig. 2*E*). This suggests that LIFU stimulation-induced long-term synaptic depression is dependent on activation of NMDARs.

LIFU stimulation does not induce neuronal activity needed to activate cFosTRAP2-mediated gene expression

Next, we attempted to measure neural activation resulting from LIFU stimulation. Because of the large size of the transducer, which occupies the space above the head of the mouse (Fig. 2*A*), we were unable to find a way to directly measure neural responses using in vivo recordings. Thus, we turned to an immunohistological method by utilizing the cFosTRAP2 mouse line (Guenthner et al., 2013). This mouse line expresses Cre-ERT2 under the activity-dependent cFos promoter; hence, it allows temporal control of Cre-dependent recombination by the timing of intraperitoneal (i. p.) injection of 4OHT, a tamoxifen analog. To visualize the activated neurons, we crossed the cFosTRAP2 with a tdTomato reporter line (Ai14). We first verified the cFosTRAP2;Ai14 mouse line by examining tdTomato induction in the visual circuit following monocular enucleation (ME). ME mice were dark exposed overnight to remove visually driven activity and brought out to light for 2 h with 4OHT injection to induce cFosTRAP2-mediated tdTomato expression. The mice were then subsequently placed back in the dark room for 7 d to prevent further visually driven activity and allow for sufficient expression of tdTomato (Guenthner et al., 2013). Fixed brain sections were counterstained with DAPI, which was used to outline different brain areas based on the anatomical landmarks that match those seen in the mouse brain atlas (Paxinos and Franklin, 2001) (Fig. 3*A*). We found significant increases in tdTomato-labeled cells in visual cortices, both V1 and V2, ipsilateral to the enucleated eye, which predominantly receive the open eye input (Fig. 3*A–C*). This result suggests that cFosTRAP2;Ai14 can indeed report the 2 h of visually driven activity. There was no significant difference in tdTomato-labeled cell density across the two hemispheres in other cortical areas examined suggesting that the cFosTRAP2;Ai14 is a good model to detect activated cells. Unfortunately, we found that the cFosTRAP2 did not drive tdTomato expression much in the dLGN. Thus, the density of labeled cells in the ipsilateral dLGN, which should have received visual activity from the open eye, was much lower than that seen in the visual cortices such that we could not detect a significant difference from that seen in the deprived contralateral dLGN. We further verified that the cFosTRAP2;Ai14 does not have baseline leakage of the cFos promoter in the absence of 4OHT. To do this we compared the tdTomato signal in normal sighted mice with and without 4OHT injection (Fig. 3*D*). We found a near absence of

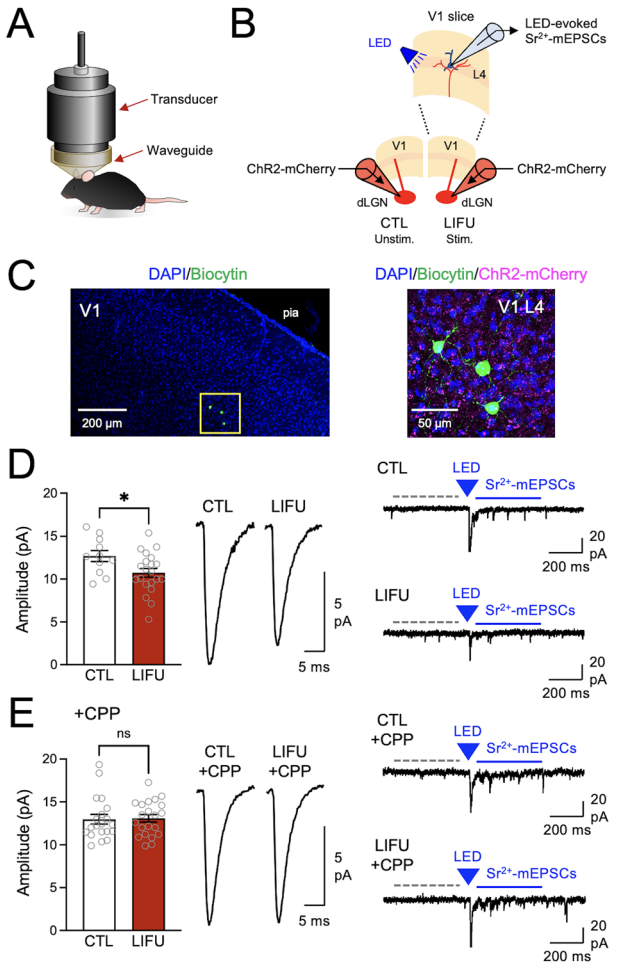

Figure 2. LIFU stimulation of dLGN results in NMDAR-dependent long-term depression of dLGN synaptic strength measured in V1 L4. ***A***, Illustration of LIFU stimulation of a mouse. The fur on the top of the head was removed to expose the skin of an anesthetized mouse, which was head-fixed on a stereotaxic frame, and the LIFU waveguide tip was firmly coupled using ultrasound gel. Mouse was enucleated at least the day before to remove any potential visually evoked responses. LIFU stimulation was delivered under isoflurane anesthesia. ***B***, Schematics of the experiment. ChR2-mCherry was expressed in dLGN of VGluT2-Cre mice at least 2 weeks before the LIFU stimulation and 6 weeks before the ex vivo brain slice electrophysiology. Whole-cell voltage-clamp recordings were done in V1 L4 principal neurons and dLGN axon terminals expressing ChR2-mCherry were activated by LED (455 nm, 5 ms pulse width) delivered through the objective lens. V1 of both hemispheres (LIFU stimulated and unstimulated CTL) were used for recording LED-evoked Sr^{2+}-mEPSCs. ***C***, An example of recorded V1 L4 neurons visualized by processing for biocytin, which was present in the internal solution. After the recording, the slice was fixed and counterstained with DAPI (blue). Three L4 neurons were recorded from this particular slice. Left, A tiled image using a 10× objective lens showing the location of the recorded cells (green). Right, A higher magnification (63×) confocal image showing the same recorded cells (green) counterstained with DAPI (blue) and overlaid with mCherry (magenta) signals showing dLGN axons expressing ChR2-mCherry. ***D***, Left, Comparison of the average amplitude of LED-evoked Sr^{2+}-mEPSCs recorded from CTL and LIFU stimulated hemispheres. The average amplitude from each V1 L4 neuron is shown as open circles and overlaid on the bars showing the group averages (mean ± SEM). $^*p < 0.05$ (two-tailed unpaired t test with Welch's correction, $t = 2.372$, $p = 0.0268$). Middle, Average traces of calculated LED-evoked Sr^{2+}-mEPSCs (see Methods for details). Right, Example recording traces (top, from a neuron in CTL hemisphere; bottom, from a neuron in LIFU stimulated hemisphere). The Gray dotted line represents the time window to measure spontaneous mEPSCs. The blue arrow denotes the time of LED stimulation (5 ms pulse duration), which is followed by an initial synchronized release mediated synaptic responses. The blue line represents the time window used to measure LED post events (started 50 ms after the LED to remove the initial synchronized release event), which include LED-evoked Sr^{2+}-mEPSCs in the background of spontaneous mEPSCs (see Methods for details on mathematical subtraction of spontaneous mEPSCs to quantify LED-evoked Sr^{2+}-mEPSCs). ***E***, Systemic application of an NMDAR antagonist (CPP, 10 mg/kg, i.p.) prevents LIFU-induced depression of LED-evoked Sr^{2+}-mEPSCs. Left, Comparison of the average amplitude of LED-evoked Sr^{2+}-mEPSCs recorded from CTL + CPP and LIFU + CPP hemispheres. The average amplitude from each V1 L4 neuron is shown as open circles and overlaid on the bars showing the group averages (mean ± SEM). CTL + CPP data set did not pass the normality test (Shapiro–Wilk test, $p = 0.0110$); hence, statistical comparison was done using a nonparametric test (two-tailed Mann–Whitney test, $p = 0.6891$). n.s., not statistically significant. Middle, Average traces of calculated LED-evoked Sr^{2+}-mEPSCs (see Methods for details). Right, Example recording traces (top, from a neuron in CTL + CPP hemisphere; bottom, from a neuron in LIFU + CPP hemisphere). Annotations are the same as in panel D.

tdTomato-positive cells in normal sighted controls without 4OHT injection when compared to those injected with 4OHT suggesting minimal baseline leakage of Cre activity in the absence of 4OHT.

We proceeded to use this mouse line for LIFU stimulation, despite very weak induction in the dLGN, based on the fact that the estimated activation spot (~2 mm in diameter and ~5 mm in length) includes the overlaying cortex and hippocampus (Fig. 1*B*), both of which show good cFosTRAP2 induction (Fig. 3) (Guenthner et al., 2013). cFosTRAP2;Ai14 mice were bilaterally enucleated the day before the LIFU stimulation to remove the visually driven activity. LIFU stimulation was done unilaterally to one hemisphere targeting the dLGN using the same parameters as used for ex vivo experiments. After 1 h of LIFU stimulation, mice received an injection of 4OHT and were kept under anesthesia for an additional 1 h to suppress neuronal activity during the time window in which cFosTRAP2 could be induced. After that, the mice recovered from anesthesia and returned to their home cage for 1 week to allow for sufficient expression of tdTomato. We analyzed the confocal images of the brain sections counterstained for DAPI, which were used to outline the anatomical boundaries (Fig. 4*A*). We first analyzed brain sections containing dLGN and outlined a 1-mm-wide rectangle (the estimated LIFU acoustic activation path) in both hemispheres, which was centered ~2 mm lateral to the midline to pass through the dLGN. We also outlined the cortex, hippocampus, and dLGN within this rectangle as additional regions of interest (ROIs) for analysis, as well as the areas corresponding to V1 in more posterior sections. Images were thresholded in the tdTomato channel to select positively labeled cells. We first plotted the cells within the rectangle ROI and quantified their depth relative to pia (Fig. 4*B*). We did not see any difference in the distribution of tdTomato-positive cells in the unstimulated (CTL) and LIFU stimulated hemispheres (Fig. 4*C*). This suggests that LIFU stimulation does not produce sufficient activity to induce cFosTRAP2 which could localize the activation spot. We also did not find any significant difference in the density of tdTomato-positive cells in the dLGN or the overlaying cortex and hippocampus in the two hemispheres (Fig. 4*D*). Neither was there a change in the tdTomato positive cell density in V1 across the two hemispheres (Fig. 4*D*).

LIFU stimulation does not produce activation of microglia

While we did not observe tissue damage due to LIFU stimulation from visual inspection of the tissue integrity and DAPI-stained images, we proceeded to examine this further by staining for IBA-1 (Fig. 5*A*), which is a marker for activated microglia associated with neuroinflammation (Hovens et al., 2014; Muzio et al., 2021). Previous studies have shown changes in the density of IBA-1 positive microglia with sensory deprivation and denervation paradigms (Fuentes-Santamaria et al., 2012; Grier et al.,

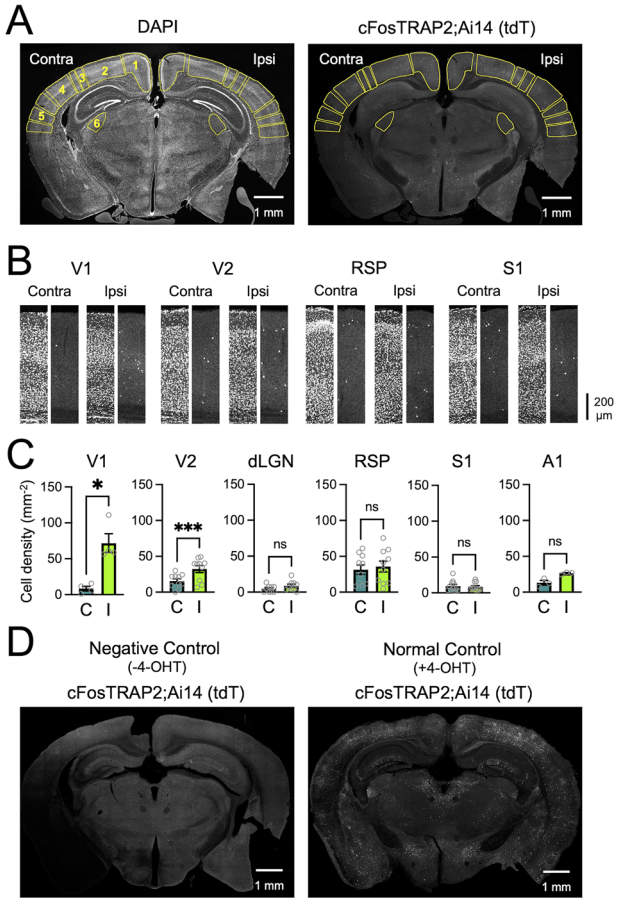

Figure 3. Validation of cFosTRAP2;Ai14 mouse. ***A***, Coronal sections of monocularly enucleated cFosTRAP2;Ai14 mice were counterstained with DAPI and confocal tiled images were taken. Using the DAPI channel, brain areas of interest were outlined by comparing the landmarks with corresponding plates in a mouse brain atlas (Paxinos and Franklin, 2001). Left, DAPI imaging with ROIs outlined. 1, retrospleneal cortex (RSP); 2, V2; 3, V1; 4, somatosensory cortex (S1); 5, auditory cortex (A1); 6, dLGN. Right, ROIs selected in the DAPI channel were used to quantify tdTomato (tdT) positive cells in each brain area. Contra, contralateral hemisphere from the enucleated eye (i.e., visually deprived hemisphere). Ipsi, ipsilateral hemisphere from the enucleated eye (i.e., dominantly driven by the open eye). Hemispheres were identified by a nick made to the bottom of one hemisphere as is visible in this image. ***B***, Zoomed-in images of each brain area from the example brain shown in (***A***). Left panels, DAPI. Right panels, tdTomato (cFosTRAP2;Ai14). Images from contra- and ipsilateral hemispheres are shown for V1, V2, RSP, and S1. ***C***, Comparison of quantified density of tdTomato positive cells in contra (***C***) and ipsi (I) hemispheres for V1, V2, dLGN, RSP, S1, and A1. Note a significant increase in tdTomatoe labeling of active cells in V1 and V2 of ipsilateral hemispheres to the enucleated eye. dLGN only showed minimal labeling in both hemispheres. cFosTRAP2-induced tdTomato cell density (mean ± SEM), Contra V1 = 8.4 ± 3.21 mm^{-2}, Ipsi V1 = 71.8 ± 13.06 mm^{-2}, $n = 4$ sections; Contra V2 = 15.5 ± 3.08 mm^{-2}, Ipsi V2 = 32.4 ± 4.90 mm^{-2}, $n = 10$ sections; Contra dLGN = 4.4 ± 1.59 mm^{-2}, Ipsi dLGN = 8.7 ± 2.32 mm^{-2}, $n = 9$ sections; Contra RSP = 31.4 ± 6.54 mm^{-2}, Ipsi RSP = 35.7 ± 7.56 mm^{-2}, $n = 10$ sections; Contra S1 = 9.4 ± 2.30 mm^{-2}, Ipsi S1 = 8.5 ± 1.68 mm^{-2}, $n = 11$ sections; Contra A1 = 13.1 ± 3.34 mm^{-2}, Ipsi A1 = 26.3 ± 1.00 mm^{-2}, $n = 3$ sections; 2 mice. $^{*}p < 0.05$, $^{**}p < 0.01$, n.s., not significant (two-tailed paired *t* tests, dLGN, $t = 1.747$, $p = 0.1187$; RSP, $t = 1.937$, $p = 0.0848$; A1, $t = 3.058$, $p = 0.0924$). Ipsi V1, Ipsi V2, and both S1 data sets did not pass the normality test (Shapiro–Wilk test, Ipsi V1 $p = 0.0108$; Ipsi V2 $p = 0.0455$; Contra S1 $p = 0.246$; Ipsi S1 $p = 0.0080$); hence, the statistical comparisons of V1, V2, and S1 tdT-positive cell densities were done using a nonparametric test (two-tailed Mann–Whitney test; V1, $p = 0.0286$; V2, $p = 0.0232$; S1, $p = 0.7969$). ***D***, Left, Image of a negative control brain section of cFosTRAP2;Ai14, which did not receive an injection of 4-OHT. There is very little background cFosTRAP2-driven tdTomato (tdT) expression. Right, Image of a control brain of a normal-sighted cFosTRAP2;Ai14, which received an injection of 4-OHT. Note induction of tdTomato across both hemispheres.

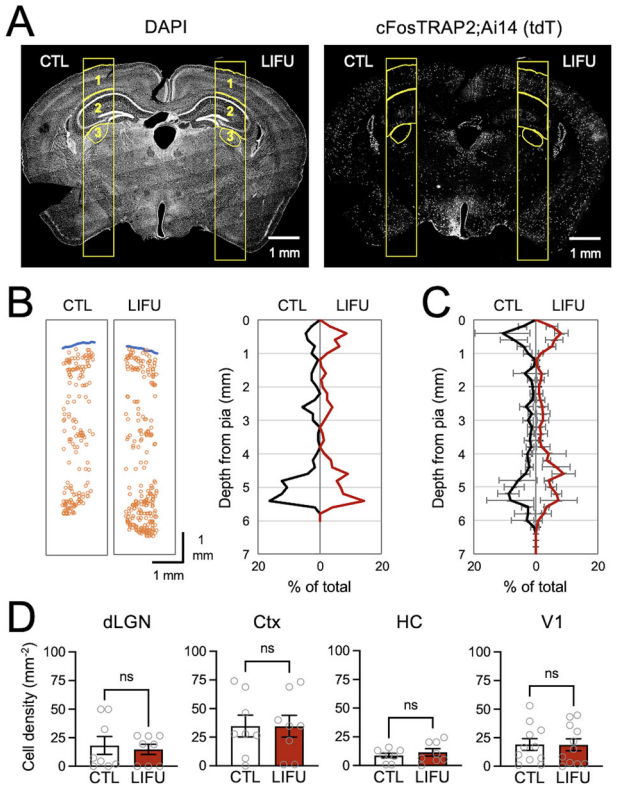

Figure 4. LIFU stimulation does not induce cFosTRAP2-driven gene expression. ***A***, Left, Unilateral LIFU stimulated cFosTRAP2;Ai14 mouse brain sections were counterstained with DAPI to identify landmarks for outlining the ROIs in the tile scanned confocal image. In sections corresponding to the LIFU target region, we outlined a 1-mm-wide rectangle that is within the predicted LIFU acoustic beam path (~2-mm diameter based on acoustic intensity measurements, see Figure 1). Within this rectangle, the overlaying cortex (Ctx, labeled 1), hippocampus (HC, labeled 2), and dLGN (labeled 3) were outlined. Right, Using the outlined ROIs from the DAPI channel, tdTomato positive cells were quantified in the tdTomato (tdT) channel. Hemispheres were identified by a nick to the bottom of one hemisphere as shown in these images. ***B***, Left, A plot showing the depth profile of identified tdT positive cells (orange circles) within the outlined rectangles in panel (***A***) for CTL and LIFU stimulated hemispheres. Blue line, pia. Right. A graph showing quantification of the depth of each tdT positive cell in relation to the outlined pia from the plot shown in the left panel. ***C***, Quantification of the depth profile of tdT positive cells across five mice with unilateral LIFU stimulation. Only the brain sections corresponding to the similar coronal plane as shown in panel (***A***) were analyzed. There was no statistical significance in the fraction of tdT positive cells across the depth between CTL and LIFU hemispheres, while there is a significant effect on the depth [two-way repeated measures ANOVA, depth × group (CTL/LIFU), F (35, 70) = 4.159, $p = 0.7851$; depth, F (35, 70) = 4.159, $p < 0.0001$]. ***D***, Quantification of the density of tdT-positive cells in dLGN, Ctx, HC, and V1. Open circles, Data from each brain section containing the specific ROI. Bars, Average tdT positive cell density (mean ± SEM, dLGN, CTL = 18.2 ± 7.83 mm^{-2}, LIFU = 14.8 ± 4.47 mm^{-2}, $n = 8$ sections; Ctx, CTL = 34.7 ± 9.46 mm^{-2}, LIFU = 34.5 ± 9.54 mm^{-2}, $n = 8$ sections; HC, CTL = 8.7 ± 1.96 mm^{-2}, LIFU = 11.5 ± 3.20 mm^{-2}, $n = 8$ sections; V1, CTL = 19.1 ± 5.10 mm^{-2}, LIFU = 18.8 ± 5.21 mm^{-2}, $n = 11$ sections) quantified from five mice. n.s., not significant (two-tailed paired *t* tests, Ctx, $t = 0.2227$, $p = 0.8347$; HC, $t = 1.131$, $p = 0.3213$; V1, $t = 0.243$, $p = 0.8200$). dLGN data sets did not pass the normality test (Shapiro–Wilk test, CTL, $p = 0.0131$; LIFU, $p = 0.0123$); hence, the statistical comparison of dLGN cell density was done using a nonparametric test (two-tailed Mann–Whitney test, $p = 0.7024$).

2016). We performed an analysis similar to that used for quantifying cFosTRAP2;Ai14 signals by outlining a rectangular ROI of 1 mm width that spans the dorsoventral thickness of the brain and is centered around 2 mm lateral to the midline to pass through the dLGN. Only brain sections that contained dLGN

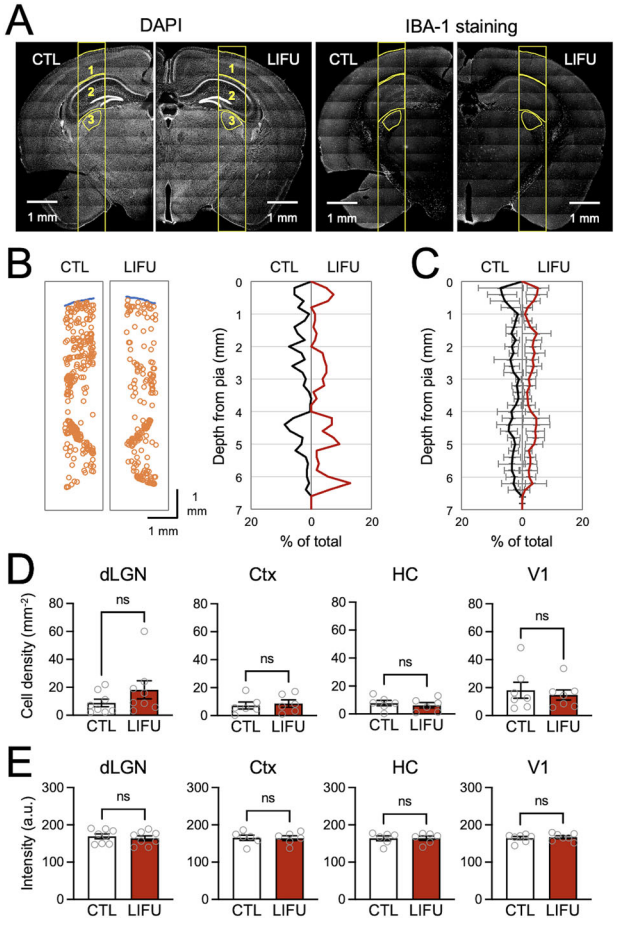

Figure 5. LIFU stimulation does not produce changes in activated microglia. ***A***, Brain sections from unilateral LIFU stimulated cFosTRAP2;Ai14 mice were stained for activated microglial marker IBA-1 and counterstained with DAPI. Left, DAPI images (10× objective lens, tiled confocal image) were used to outline the ROIs as described above. Right, The ROIs were then used for quantifying the IBA-1 images. In this particular example, images from each hemisphere were saved as different image files, hence displayed as separate panels. Hemispheres were identified by a nick to the bottom of one side as shown. ***B***, Left, A plot showing the depth profile of identified IBA-1 positive cells (orange circles) within the outlined rectangles in panel (***A***) for CTL and LIFU stimulated hemispheres. Blue line, pia. Right, A graph showing quantification of the depth of each IBA-1 positive cell in relation to the outlined pia from the plot shown in the left panel. ***C***, Quantification of the depth profile of IBA-1 positive cells across 5 mice with unilateral LIFU stimulation. Only the brain sections corresponding to the similar coronal plane as shown in panel (***A***) were analyzed. There was no statistical significance in the fraction of IBA-1 positive cells across the depth between CTL and LIFU hemispheres, while there was a significant effect of the depth [two-way repeated measures ANOVA, depth × group (CTL/LIFU), $F(35, 560) = 0.5992$, $p = 0.9682$; depth, $F(5.277, 84.43) = 5.027$, $p = 0.0003$]. ***D***, Quantification of the density of IBA-1 positive cells in dLGN, Ctx, HC, and V1. Open circles, Data from each brain section containing the specific ROI. Bars, Average IBA-1 positive cell density (mean ± SEM, dLGN, CTL = 8.8 ± 18.19 mm^{-2}, LIFU = 18.2 ± 6.48 mm^{-2}, $n = 8$ sections; Ctx, CTL = 7.2 ± 2.48 mm^{-2}, LIFU = 8.6 ± 2.63 mm^{-2}, $n = 6$ sections; HC, CTL = 7.7 ± 1.92 mm^{-2}, LIFU = 6.2 ± 1.93 mm^{-2}, $n = 6$ sections; V1, CTL = 18.1 ± 5.74 mm^{-2}, LIFU = 14.8 ± 3.64 mm^{-2}, $n = 7$ sections) quantified from five mice. n.s., not significant (two-tailed paired t tests, Ctx, $t = 1.161$, $p = 0.2980$; HC, $t = 0.9803$, $p = 0.3824$; V1, $t = 0.5349$, $p = 0.6298$). dLGN LIFU data set did not pass the normality test (Shapiro–Wilk test, $p = 0.0121$); hence, the statistical comparison of dLGN cell density was done using a nonparametric test (two-tailed Mann–Whitney test, $p = 0.1605$). Two data points for Ctx were removed based on an outlier test (ROUT, Q = 1%), but the inclusion of these data points does not alter the conclusion (two-tailed paired t test, $t = 0.7689$, $p = 0.4671$). ***E***, Quantification of the intensity (a.u., arbitrary unit of fluorescence intensity) of IBA-1 positive cells in dLGN, Ctx, HC, and V1. Open circles, Data from each brain section containing the specific ROI. Bars, Average IBA-1 positive cell intensity (mean ± SEM, dLGN, CTL = 169 ± 6.5 a.u., LIFU = 164 ± 6.6 a.u., $n = 8$ sections; Ctx, CTL = 165 ± 7.0 a.u., LIFU = 164 ± 6.6 a.u., $n = 6$ sections; HC, CTL = 164 ± 6.4 a.u., LIFU = 164 ± 5.8 a.u., $n = 6$ sections; V1, CTL = 165 ± 4.1 a.u., LIFU = 167 ± 3.8 a.u., $n = 7$ sections) quantified from five mice. n.s., not significant (two-tailed paired t tests, dLGN, $t = 0.3307$, $p = 0.7574$; Ctx, $t = 0.6487$, $p = 0.5519$; HC, $t = 0.2322$, $p = 0.8278$; V1, $t = 0.3281$, $p = 0.7644$).

were analyzed for comparison of the distribution of IBA-1 positive microglia across the depth from pia (Fig. 5*B*,*C*). We did not observe a significant difference in their distribution profile across the depth between the unstimulated and LIFU stimulated hemispheres (Fig. 5*C*). We further analyzed the density of IBA-1 positive microglia in each brain region of interest, as well as the IBA-1 intensity, and did not find any significant difference between the two hemispheres (Fig. 5*D*,*E*). We did notice a tendency of an increase in IBA-1 positive cell density in dLGN of LIFU stimulated hemisphere, which did not reach statistical significance.

Simulation of predicted neuronal activity in dLGN with LIFU stimulation

Since we were unable to detect neuronal activation with LIFU stimulation using the cFosTRAP2-mediated gene expression system, we turned to simulations to see what type of neuronal activity is predicted from our stimulation parameters. There are many models and hypotheses on how ultrasound could activate neurons (Dell'Italia et al., 2022), but we decided to utilize a biophysics-based model that can produce clear predictions on physiological neuronal output. One such model is multi-scale optimized neuronal intramembrane cavitation (SONIC) (Lemaire et al., 2019), which is based on the neuronal intramembrane cavitation excitation (NICE) model of ultrasound activation (Plaksin et al., 2014, 2016). According to the NICE model, ultrasound-induced neuronal activation is due to oscillations of small areas (submicron-sized) of membranes, which are called bilayer sonophores (Krasovitski et al., 2011). It is hypothesized that these sonophores provide mechanoelectrical coupling that induces membrane currents that can lead to the depolarization of neurons to generate action potentials (Plaksin et al., 2014). The predictions of the NICE model are consistent with the basic observations of ultrasound stimulation studies showing that effective stimulation of cortical neurons requires long durations of continuous wave stimulation over pulse stimulation (Tufail et al., 2010, 2011; King et al., 2013). The SONIC model is a revised version of the NICE model that is optimized to be computationally more efficient (Lemaire et al., 2019).

We used the SONIC model to simulate the activity of dLGN neurons under the LIFU stimulation parameters utilized for our study. Importantly, the SONIC model contains built-in parameters for simulating thalamocortical neurons, which include T-type Ca^{2+} channels (see Methods for details of the model). Because thalamocortical neurons exhibit different firing states (tonic and burst modes) due to their T-type Ca^{2+} channels, we ran our simulations using two distinct values of resting membrane potential (each artificially constrained by a specific driving current), −55 mV for tonic mode and −70 mV for burst mode, to allow predictions of neuronal activity under the two different states. We found that in the different modes, the same LIFU stimulation parameters result in different predicted firing patterns and intracellular Ca^{2+} transients (Fig. 6). Under the tonic

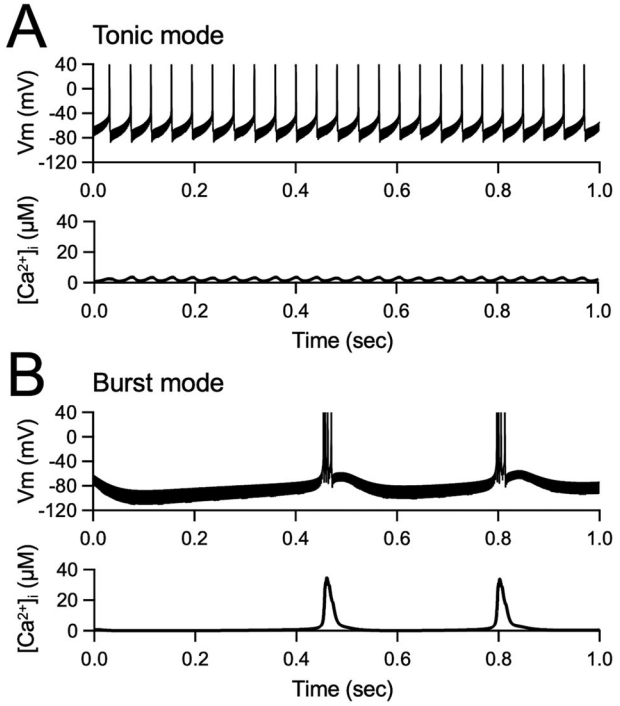

Figure 6. Simulation of predicted neuronal activity in dLGN with LIFU stimulation parameters used experimentally. ***A***, Results from simulation in the SONIC model using the parameters for dLGN when in a depolarized tonic firing mode. Top, Predicted membrane potential (Vm) changes show a train of single action potentials at ~25 Hz. Bottom, Predicted intracellular Ca^{2+} concentration. ***B***, Results from simulation in the SONIC model using the parameters for dLGN when in a hyperpolarized burst firing mode. Top, Predicted membrane potential (Vm) changes show bursts of action potentials repeated at ~250 msec inter-burst interval. Bottom, Predicted intracellular Ca^{2+} concentration. See Table 1 for the details on ionic conductances used for the simulation.

mode, the model predicted a train of action potentials at around 25 Hz with corresponding small increases in intracellular Ca^{2+} transients (~3 μM peak increases in concentration) (Fig. 6*A*). With the burst mode simulation, it predicted the generation of bursts repeated at roughly 250 msec inter-burst intervals with corresponding higher increases in intracellular Ca^{2+} concentration (~35 μM peak) (Fig. 6*B*). The simulation results suggest that the neuromodulation of dLGN activity by LIFU is state dependent but has a range of single spiking activity under tonic mode that could in principle drive LTD in the postsynaptic V1 neurons.

Discussion

Here, we report that transcranial LIFU stimulation of a deep brain structure, dLGN, produces long-lasting weakening of dLGN synaptic strength onto V1 L4 neurons in adult mice, which was dependent on NMDAR activation (Fig. 2). LIFU stimulation did not produce neural activity levels sufficient to drive cFosTRAP2-induce gene expression (Fig. 4) or activation of microglia as visualized by IBA-1 staining (Fig. 5). Using the SONIC model (Lemaire et al., 2019), which is based on the neuronal intramembrane cavitation theory of ultrasound neuronal activation (Plaksin et al., 2014, 2016), we found that the particular LIFU stimulation parameters used in our study are predicted to generate different patterns of activity dependent on the state of the dLGN neuron. The model predicts a train of action potentials around 25 Hz under tonic firing mode, while a series of short bursts repeated around 4 Hz under burst firing mode (Fig. 6).

Observation of synaptic plasticity after tFUS is not unique to our system. A recent study demonstrated that tFUS produces synaptic depression in the hippocampal CA1 of adult rats, which was rather transient and lasted about 20–60 min (Niu et al., 2022). There is also a report where tFUS of the motor cortex (M1) in human subjects shows potentiation of TMS-evoked motor evoked potentials (MEPs) for at least an hour (Zhang et al., 2021), but whether such plasticity was due to synaptic plasticity or changes in neuronal excitability was not determined. The novelty of our study is that we observed long-lasting synaptic depression of TC inputs to V1 in adult mice, which was measured at least 2 weeks after the LIFU stimulation. Unlike the CA1 or M1, which exhibits robust synaptic plasticity throughout the lifespan of rodents (Hess and Donoghue, 1996; Kumar, 2011), TC synapses in V1 display an early critical period which closes around the third postnatal week (Jiang et al., 2007) and is absent in adults (Rodriguez et al., 2018). The percentage of synaptic depression observed in our study with LIFU stimulation (~15%) is comparable to the magnitude of LTD observed at TC synapses measured ex vivo in V1 L4 of young juvenile mice (P18–23) (Jiang et al., 2007). The developmental loss of long-term synaptic plasticity in the dLGN to V1 synapses has been suggested to be correlated with the diminished experience-dependent plasticity in the adult V1 (Lee and Whitt, 2015). As such, recovery of TC plasticity in the adult V1 has been considered critical for recovering juvenile-like ocular dominance plasticity (Montey and Quinlan, 2011) or accelerating the adult form of it (Rodriguez et al., 2018) in rodents. Therefore, our observation that a noninvasive transcranial LIFU stimulation can result in LTD of TC synapses in the adult V1 paves a way for developing new noninvasive therapies that could potentially help recover adult V1 functionality.

One of the remaining questions is how LIFU stimulation leads to the long-term synaptic plasticity we observe here. Due to the size of the LIFU transducer used in this study, we were unable to directly measure neuronal activity in vivo using conventional electrophysiological recording techniques or in vivo two-photon Ca^{2+} imaging. Instead, we utilized an immunohistochemical method of visualizing activated neurons using the cFosTRAP2 mouse line (Guenthner et al., 2013). While we were able to visualize activated neurons in visual cortices following monocular visual stimulation (Fig. 3), we were unable to see differences in labeled active neurons between the LIFU stimulated and unstimulated control hemispheres (Fig. 4). This could suggest the following several possibilities: (1) our LIFU stimulation protocol does not activate neurons; (2) it produces neuronal activity, but it falls below the activity threshold for cFos promoter activation; or (3) it only provides subthreshold neuromodulation. To clearly distinguish between these possibilities, further studies will need to be done to directly measure neuronal activity ideally using intracellular recording techniques to discern even subthreshold or hyperpolarization events that may accompany tFUS. However, our observation that the LTD of dLGN inputs V1 L4 is dependent on NMDAR activity (Fig. 2*E*) suggests that LIFU stimulation would have caused some level of neural activity that can activate NMDARs in the range for LTD induction. While the parameter space for inducing LTD of TC synapses even in juvenile V1 has not been fully characterized, it is expected to be similar to the range (1–10 Hz) seen in L4 to L2/3 synapses ex vivo (Kirkwood et al., 1996). It is known that cFos induction requires a threshold of higher activity, in particular, repeated

trains of high-frequency stimulation (100–400 Hz) used for generating late-phase LTP (L-LTP) is most effective (Dragunow et al., 1989; Nikolaev et al., 1991; Kaczmarek, 1992). Thus, our results suggest that the LIFU stimulation used in this study would have produced a moderate level of prolonged activity that is below the cFosTRAP2 induction threshold. We used the SONIC model to simulate the effect of our LIFU stimulation parameters on a model dLGN neuron and saw that the expected activity is dependent on the state of the dLGN neuronal firing mode. dLGN neurons express T-type Ca^{2+} channels, which allows them to generate tonic firing at depolarized up-state or produce burst firing when hyperpolarized as would occur during down states (Sherman, 2001). The predicted firing frequency under tonic mode is in line with stimulation parameters that could produce LTD, while under burst mode it would mimic a θ-burst stimulation pattern which is known to be effective at driving LTP at dLGN to V1 synapses in adult rats (Heynen and Bear, 2001). Our simulation results suggest that the outcome of LIFU stimulation will depend on the state of the thalamic neurons. Based on our observations of an LTD at TC synapses and no significant change in cFosTRAP2 induction, we could speculate that dLGN neurons might have been kept at a depolarized tonic firing mode during our LIFU stimulation. While ultrasound sonication can result in temperature increases, it is likely negligible under LIFU stimulation parameters (calculated to be <0.1°C in published studies) (Yu et al., 2021; Niu et al., 2022). Increasing the temperature has been shown to reduce the excitability of dLGN neurons ex vivo (Van Hook, 2020); hence, if there was LIFU sonication-induced heat, it would act to reduce the overall neuronal activity compared to what is predicted. We acknowledge that the neuronal intramembrane cavitation theory is just one of many models developed to account for potential mechanisms of tFUS neuromodulation (Dell'Italia et al., 2022). However, because the SONIC model is built using biophysical parameters of model neurons, it has the potential to be experimentally tested if the single-cell level activity or intracellular Ca^{2+} transient measures can be done with LIFU stimulations. This will require the development of transducers that can be used in conjunction with in vivo intracellular recordings or Ca^{2+} imaging in mice, which will become possible based on recent efforts on miniaturization (Kim et al., 2019; Jo et al., 2022; Kook et al., 2023).

Disclaimer

This material is based on work while one of the authors (G.M.H.) was supported by (while serving at) the National Science Foundation. Any opinions, findings, conclusions, or recommendations expressed in this material are those of the authors and do not necessarily reflect the views of the National Science Foundation. This article was prepared while Dr. Grace Hwang was employed at Johns Hopkins University. The opinions expressed in this article are the author's own and do not reflect the view of the National Institutes of Health, the Department of Health and Human Services, or the United States Government.

References

Baek H, Pahk KJ, Kim H (2017) A review of low-intensity focused ultrasound for neuromodulation. Biomed Eng Lett 7:135–142.

Barkat TR, Polley DB, Hensch TK (2011) A critical period for auditory thalamocortical connectivity. Nat Neurosci 14:1189–1194.

Chokshi V, Gao M, Grier BD, Owens A, Wang H, Worley PF, Lee HK (2019) Input-specific metaplasticity in the visual cortex requires homer1a-mediated mGluR5 signaling. Neuron 104:736–748 e736.

Chung S, Jeong JH, Ko S, Yu X, Kim YH, Isaac JTR, Koretsky AP (2017) Peripheral sensory deprivation restores critical-period-like plasticity to adult somatosensory thalamocortical inputs. Cell Rep 19:2707–2717.

Coleman JE, Nahmani M, Gavornik JP, Haslinger R, Heynen AJ, Erisir A, Bear MF (2010) Rapid structural remodeling of thalamocortical synapses parallels experience-dependent functional plasticity in mouse primary visual cortex. J Neurosci 30:9670–9682.

Crair MC, Malenka RC (1995) A critical period for long-term potentiation at thalamocortical synapses. Nature 375:325–328.

Dell'Italia J, Sanguinetti JL, Monti MM, Bystritsky A, Reggente N (2022) Current state of potential mechanisms supporting low intensity focused ultrasound for neuromodulation. Front Hum Neurosci 16:872639.

Desai NS, Cudmore RH, Nelson SB, Turrigiano GG (2002) Critical periods for experience-dependent synaptic scaling in visual cortex. Nat Neurosci 5: 783–789.

Destexhe A, Bal T, McCormick DA, Sejnowski TJ (1996) Ionic mechanisms underlying synchronized oscillations and propagating waves in a model of ferret thalamic slices. J Neurophysiol 76:2049–2070.

Dragunow M, Abraham WC, Goulding M, Mason SE, Robertson HA, Faull RL (1989) Long-term potentiation and the induction of c-fos mRNA and proteins in the dentate gyrus of unanesthetized rats. Neurosci Lett 101:274–280.

Dudek SM, Friedlander MJ (1996) Developmental down-regulation of LTD in cortical layer IV and its independence of modulation by inhibition. Neuron 16:1097–1106.

Feldman DE, Nicoll RA, Malenka RC, Isaac JT (1998) Long-term depression at thalamocortical synapses in developing rat somatosensory cortex. Neuron 21:347–357.

Fuentes-Santamaria V, Alvarado JC, Juiz JM (2012) Long-term interaction between microglial cells and cochlear nucleus neurons after bilateral cochlear ablation. J Comp Neurol 520:2974–2990.

Goel A, Lee HK (2007) Persistence of experience-induced homeostatic synaptic plasticity through adulthood in superficial layers of mouse visual cortex. J Neurosci 27:6692–6700.

Grier BD, Belluscio L, Cheetham CE (2016) Olfactory sensory activity modulates microglial-neuronal interactions during dopaminergic cell loss in the olfactory bulb. Front Cell Neurosci 10:178.

Guenthner CJ, Miyamichi K, Yang HH, Heller HC, Luo L (2013) Permanent genetic access to transiently active neurons via TRAP: targeted recombination in active populations. Neuron 78:773–784.

Hess G, Donoghue JP (1996) Long-term potentiation and long-term depression of horizontal connections in rat motor cortex. Acta Neurobiol Exp (Wars) 56:397–405.

Heynen AJ, Bear MF (2001) Long-term potentiation of thalamocortical transmission in the adult visual cortex in vivo. J Neurosci 21:9801–9813.

Hooks BM, Chen C (2020) Circuitry underlying experience-dependent plasticity in the mouse visual system. Neuron 106:21–36.

Hovens IB, Nyakas C, Schoemaker RG (2014) A novel method for evaluating microglial activation using ionized calcium-binding adaptor protein-1 staining: cell body to cell size ratio. Neuroimmunol Neuroinflammation 1:82–88.

Huguenard JR, McCormick DA (1992) Simulation of the currents involved in rhythmic oscillations in thalamic relay neurons. J Neurophysiol 68:1373–1383.

Hwang GM, Lani SW, Rosenberg AP, Congedo MB, Tyler WJ (2018) Forward-looking engineering concepts for ultrasonic modulation of neural circuit activity in humans. Proc. SPIE, 10639:106391J.

Jiang B, Trevino M, Kirkwood A (2007) Sequential development of long-term potentiation and depression in different layers of the mouse visual cortex. J Neurosci 27:9648–9652.

Jo Y, et al. (2022) General-purpose ultrasound neuromodulation system for chronic. Closed-loop preclinical studies in freely behaving rodents. Adv Sci (Weinh) 9:e2202345.

Kaczmarek L (1992) Expression of c-fos and other genes encoding transcription factors in long-term potentiation. Behav Neural Biol 57: 263–266.

Kim H, Kim S, Sim NS, Pasquinelli C, Thielscher A, Lee JH, Lee HJ (2019) Miniature ultrasound ring array transducers for transcranial ultrasound neuromodulation of freely-moving small animals. Brain Stimul 12:251–255.

King RL, Brown JR, Newsome WT, Pauly KB (2013) Effective parameters for ultrasound-induced in vivo neurostimulation. Ultrasound Med Biol 39: 312–331.

Kirkwood A, Rioult MC, Bear MF (1996) Experience-dependent modification of synaptic plasticity in visual cortex. Nature 381:526–528.
Kook G, Jo Y, Oh C, Liang X, Kim J, Lee SM, Kim S, Choi JW, Lee HJ (2023) Multifocal skull-compensated transcranial focused ultrasound system for neuromodulation applications based on acoustic holography. Microsyst Nanoeng 9:45.
Krasovitski B, Frenkel V, Shoham S, Kimmel E (2011) Intramembrane cavitation as a unifying mechanism for ultrasound-induced bioeffects. Proc Natl Acad Sci U S A 108:3258–3263.
Kumar A (2011) Long-term potentiation at CA3-CA1 hippocampal synapses with special emphasis on aging, disease, and stress. Front Aging Neurosci 3:7.
Lani SW, Congedo M, Hwang G, Rosenberg A (2018) Acoustical experimental design for ultrasonic neurostimulation on rodents. J Acoust Soc Am 143:1732.
Lani SW, Rosenberg AP, Magruder S, Hwang GM (2017) Frequency-agile, low-intensity, broadband ultrasonic array as a brain computer interface technology for improving neurological health. Society for Neuroscience Abstracts 528.09.
Lee H-K, Choi SY, Kirkwood A (2005) Critical Periods of Cortical Plasticity. In: *Early interventions: Biomedical & Social Perspectives* (Accardo PJ, O'Connor-Leppert ML, Lipkin PH, Rogers BT, eds). Timonium, MD: York Press.
Lee HK, Whitt JL (2015) Cross-modal synaptic plasticity in adult primary sensory cortices. Curr Opin Neurobiol 35:119–126.
Lemaire T, Neufeld E, Kuster N, Micera S (2019) Understanding ultrasound neuromodulation using a computationally efficient and interpretable model of intramembrane cavitation. J Neural Eng 16:046007.
FDA (2023) Marketing clearance of diagnostic ultrasound systems and transducers. Guidance for industry and food and drug administration staff.
Montey KL, Quinlan EM (2011) Recovery from chronic monocular deprivation following reactivation of thalamocortical plasticity by dark exposure. Nat Commun 2:317.
Muzio L, Viotti A, Martino G (2021) Microglia in neuroinflammation and neurodegeneration: from understanding to therapy. Front Neurosci 15: 742065.
Nikolaev E, Tischmeyer W, Krug M, Matthies H, Kaczmarek L (1991) c-fos protooncogene expression in rat hippocampus and entorhinal cortex following tetanic stimulation of the perforant path. Brain Res 560:346–349.
Niu X, Yu K, He B (2022) Transcranial focused ultrasound induces sustained synaptic plasticity in rat hippocampus. Brain Stimul 15:352–359.
Paxinos G, Franklin KBJ (2001) *The mouse brain in streotaxic coordinates*, Ed 2. San Diego, USA: Academic Press.
Petrus E, Isaiah A, Jones AP, Li D, Wang H, Lee HK, Kanold PO (2014) Crossmodal induction of thalamocortical potentiation leads to enhanced information processing in the auditory cortex. Neuron 81:664–673.
Petrus E, Rodriguez G, Patterson R, Connor B, Kanold PO, Lee HK (2015) Vision loss shifts the balance of feedforward and intracortical circuits in opposite directions in mouse primary auditory and visual cortices. J Neurosci 35:8790–8801.
Plaksin M, Kimmel E, Shoham S (2016) Cell-type-selective effects of intramembrane cavitation as a unifying theoretical framework for ultrasonic neuromodulation. eNeuro 3:e0136-15.2016.
Plaksin M, Shoham S, Kimmel E (2014) Intramembrane cavitation as a predictive bio-piezoelectric mechanism for ultrasonic brain stimulation. Phys Rev X4:011004.
Pospischil M, Toledo-Rodriguez M, Monier C, Piwkowska Z, Bal T, Fregnac Y, Markram H, Destexhe A (2008) Minimal Hodgkin–Huxley type models for different classes of cortical and thalamic neurons. Biol Cybern 99: 427–441.
Rodriguez G, Chakraborty D, Schrode KM, Saha R, Uribe I, Lauer AM, Lee HK (2018) Cross-modal reinstatement of thalamocortical plasticity accelerates ocular dominance plasticity in adult mice. Cell Rep 24:3433–3440 e3434.
Sherman SM (2001) Tonic and burst firing: dual modes of thalamocortical relay. Trends Neurosci 24:122–126.
Siebner HR, Hartwigsen G, Kassuba T, Rothwell JC (2009) How does transcranial magnetic stimulation modify neuronal activity in the brain? Implications for studies of cognition. Cortex 45:1035–1042.
Thielscher A, Kammer T (2002) Linking physics with physiology in TMS: a sphere field model to determine the cortical stimulation site in TMS. NeuroImage 17:1117–1130.
Tufail Y, Matyushov A, Baldwin N, Tauchmann ML, Georges J, Yoshihiro A, Tillery SI, Tyler WJ (2010) Transcranial pulsed ultrasound stimulates intact brain circuits. Neuron 66:681–694.
Tufail Y, Yoshihiro A, Pati S, Li MM, Tyler WJ (2011) Ultrasonic neuromodulation by brain stimulation with transcranial ultrasound. Nat Protoc 6: 1453–1470.
Tyler WJ (2011) Noninvasive neuromodulation with ultrasound? a continuum mechanics hypothesis. Neuroscientist 17:25–36.
Tyler WJ, Lani SW, Hwang GM (2018) Ultrasonic modulation of neural circuit activity. Curr Opin Neurobiol 50:222–231.
Van Hook MJ (2020) Temperature effects on synaptic transmission and neuronal function in the visual thalamus. PLoS One 15:e0232451.
Wagner T, Valero-Cabre A, Pascual-Leone A (2007) Noninvasive human brain stimulation. Annu Rev Biomed Eng 9:527–565.
Woods AJ, et al. (2016) A technical guide to tDCS, and related non-invasive brain stimulation tools. Clin Neurophysiol 127:1031–1048.
Yoo SS, Bystritsky A, Lee JH, Zhang Y, Fischer K, Min BK, McDannold NJ, Pascual-Leone A, Jolesz FA (2011) Focused ultrasound modulates region-specific brain activity. NeuroImage 56:1267–1275.
Yu X, Chung S, Chen DY, Wang S, Dodd SJ, Walters JR, Isaac JT, Koretsky AP (2012) Thalamocortical inputs show post-critical-period plasticity. Neuron 74:731–742.
Yu K, Niu X, Krook-Magnuson E, He B (2021) Intrinsic functional neuron-type selectivity of transcranial focused ultrasound neuromodulation. Nat Commun 12:2519.
Zhang Y, Ren L, Liu K, Tong S, Yuan TF, Sun J (2021) Transcranial ultrasound stimulation of the human motor cortex. iScience 24:103429.